VLASS Project Memo: 18

Characterization of VLASS Single Epoch Cube Validation Products

M. Lacy

October 25, 2022

Abstract

This Memo describes the validation of the VLASS SE cube images with respect to the survey requirements. We show that, based on test cubes and other analysis, the survey is likely to meet its requirements for polarimetric and spectroscopic accuracy, though more work is needed to characterize a large sample of cubes, once they are available from the pipeline.

1 Background

1.1 VLASS cubes

The wide bandwidth of VLASS means that, in order to avoid bandwidth depolarization for polarimetric studies of objects with Faraday Rotation Measure (RM) $\gtrsim 100$, the 2 GHz band needs to be split into smaller chunks. The original plan for VLASS Single Epoch processing envisaged making 16-plane cubes with 128 MHz channel width for the purpose of being able to measure polarization for objects with $RM \gtrsim 1000$.

Cubes also enable in-band spectral index maps of extended objects to be made without concerns about w-terms in the imaging, which, if uncorrected, result in chromatic aberration-like effects in wide-band tt1 continuum images (VLASS Memo 14).[1] These aberrations become significant for VLASS data taken at high zenith distances ($\gtrsim 45°$) and imaged with the mosaic gridder. At the time of writing it is not clear if imaging with the the AW-project gridder that corrects these effects will be viable for VLASS, so cube-based spectral index maps may be needed for high zenith distance observations (typically in the South of the survey).

For both the polarization and spectral index use cases there is a trade-off between having a few wide channels or many narrow ones. Wide channels clean well, but for spectral indices will not have as accurate position corrections, and for polarization will not be as sensitive to high RMs. Narrow channels result in more accurate spectral indices and polarizations for high signal-to-noise objects, but lower accuracy measurements for faint objects due to the relatively shallow clean depth that can be achieved. We therefore tried out a number of different channel combinations during the validation process, as detailed in Section 2.1.

1.2 Frequency-dependent position corrections

The position correction that needs to be applied to VLASS data to compensate for the lack of w-terms in the imaging algorithm is inversely proportional to the square of the frequency. We therefore applied a different position correction to each plane of the cube based on the central frequency of each channel, as detailed in Memo 14, prior to the analysis shown below. See VLASS Memo 14 for a discussion of the resulting astrometric accuracy.

1.3 Polarization calibration in the circular basis

The Stokes parameters I, Q, U, V are related to the correlations $<RR>, <LL>, <RL>, <LR>$ via:

$$I = <RR> + <LL> \quad (1)$$

[1] VLASS Memos are available from https://library.nrao.edu/vlass.shtml

$$Q = \frac{1}{2}(< RL > + < LR >) \tag{2}$$

$$U = \frac{1}{2i}(< RL > - < LR >) \tag{3}$$

$$V =< RR > - < LL > \tag{4}$$

(e.g. Hales, 2017). The individual Stokes images, then, are constructed from different combinations of the cross- and parallel-hand correlations. Leakage from L to R and vice-versa needs to be calibrated out (see Appendix). Also the delay and phase difference between R and L as a function of frequency needs to be determined. This constitutes the on-axis polarization calibration. For most of VLASS, except VLASS 1.1, the leakage terms ("D-terms") were derived through observations of a bright, unpolarized point source (so any polarization seen is due to leakage). This enables the polarization leakage terms to be corrected as a function of frequency. This is referred to as the "Df" solution in CASA. In VLASS 1.1, most SBs were calibrated by repeat observations of a polarized point-source calibrator over a parallactic angle range of >90 deg. This allows the polarization of the source to be separated from the leakage terms (the "Df+QU" solution). As it was hard to ensure the parallactic angle coverage in a VLASS SB given the dynamic scheduling of VLASS this method was not used from the VLASS 1.2 campaigns onwards. Both methods provide comparable calibration accuracy (Hales, 2017).

In addition to the on-axis calibration, the VLA primary beam also has a polarization response that varies with position within the primary beam. These off-axis terms can also lead to spurious polarizations.

2 Cube choices

2.1 Channel placements and widths

The original design of the VLASS coarse cubes had a nominal 16 planes corresponding to the 16×128 MHz spectral windows of a VLASS observation (though 1–2 of these are usually completely flagged due to RFI). We also compare to a four-plane cube each containing four spectral windows, and a hybrid solution that has individual spectral windows in the lower sideband, and combines spectral windows in the upper sideband. The advantage of increasing the channel width, especially at high frequencies, is that the signal-to-noise of a source in each plane is improved for steep spectrum sources, leading to better cleaning and fewer issues from clean bias (which is more important in the cubes than in the SE continuum images due to the higher PSF sidelobes in the cube data). The wider the channels, however, the more depolarization there is across them, and the more smearing of the beam due to w-plane effects (both scale as wavelength squared). The characteristics of each cube design are shown in Table 1.

C. van Eck (personal communication) has calculated the loss of polarization signal as a function of RM for the three cube options (Figure 1). 10% losses occur at RMs of approximately 120, 300 and 500 for the 4-plane, variable-plane and 16-plane options, respectively. Based on discussions with the Survey Science Group (SSG), it was decided that the original 16-plane cubes should be made to minimize in-band depolarization, however, we retain the analysis of the other cube options in this Memo for completeness.

Table 1: Cube channelizations

Cube design	Nominal # of channels	Typical # of channels	Channel widths	$RM_{\pi}^{\dagger}$
16-plane	16	11-13	16×128 MHz	1138-8387
4-plane	4	4	4×512 MHz	364-1789
11-plane	11	7-9	8× 128,256,256,512	1138-1789

† $RM_{\pi} = \pi/(\lambda_1^2 - \lambda_2^2)$ is the amount of rotation measure needed to rotate a polarization vector by π radians between the starting wavelength of the channel, λ_1, and the ending wavelength, λ_2.

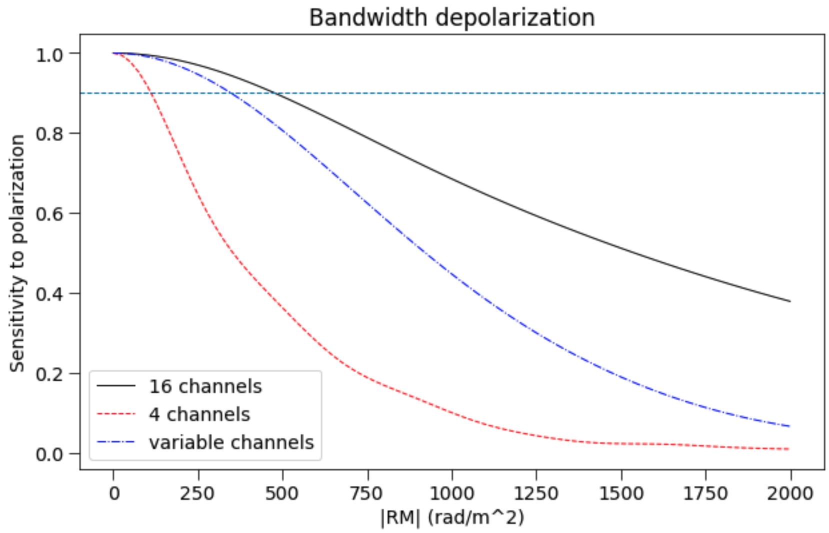

Figure 1: Loss of polarization signal as a function of RM for the three cube options. (Figure courtesy of Cameron van Eck.)

2.1.1 System noise as a function of frequency

EVLA Memo 204 (Momjian 2017)[2] shows a plot of the the System Equivalent Flux Density (SEFD) across S-band. RMS is related to SEFD though:

$$RMS(Jy) = \frac{1}{\eta_c} \frac{SEFD}{\sqrt{\beta \tau n_{pol} N(N-1)}} \tag{5}$$

where β is the channel width in Hz, τ is the integration time in seconds (5.2s for VLASS; see the Technical Implementation Plan), $N = 25$ is the typical number of antennas, n_{pol} is the number of polarizations (two, corresponding to RR and LL for VLASS) and η_c is the correlator efficiency (0.936 for 8-bit). We can therefore estimate the noise per channel in the absence of RFI.

2.1.2 Measured noise and RFI characteristics

For our initial analysis we picked the cube J032647-283000 in the ECDFS field that had a bright FRII source (0328-2830) that can be used for spectral index and polarization validation. We measured the median of each of the RMS images for the three cube designs. The results are shown in Figure 2, where we also plot the expected noise from Equation 5 using the interpolated SEFD at the band center and the width of each channel. The results show that the observed noise is reasonably close to the expected noise (within $\sim 50\%$) except for spw 4 at 2.3 GHz, which is badly affected by RFI, and the higher frequencies, especially spws 16 and 17, which again are badly affected by RFI.

Most of the RFI seen in S-band is from satellites. Schinzel (2018; EVLA Memo 206) shows that most RFI is seen in the ranges 2.16–2.54 GHz and 3.7–4 GHz, affecting VLASS spectral windows 3, 4, 5, 16 and 17. This is consistent with the appearance of Figure 2, where spectral window 3 (2.156 GHz) is completely flagged and spectral windows 4, 16 and 17 (2.284 GHz, 3.372 GHz and 3.756 GHz, respectively) are very noisy. Overall then, we expect somewhere between 10-30% of the band to be lost to RFI, depending on sky position, including one or more entire cube planes.

[2]EVLA Memos are available from `https://library.nrao.edu/evla.shtml`

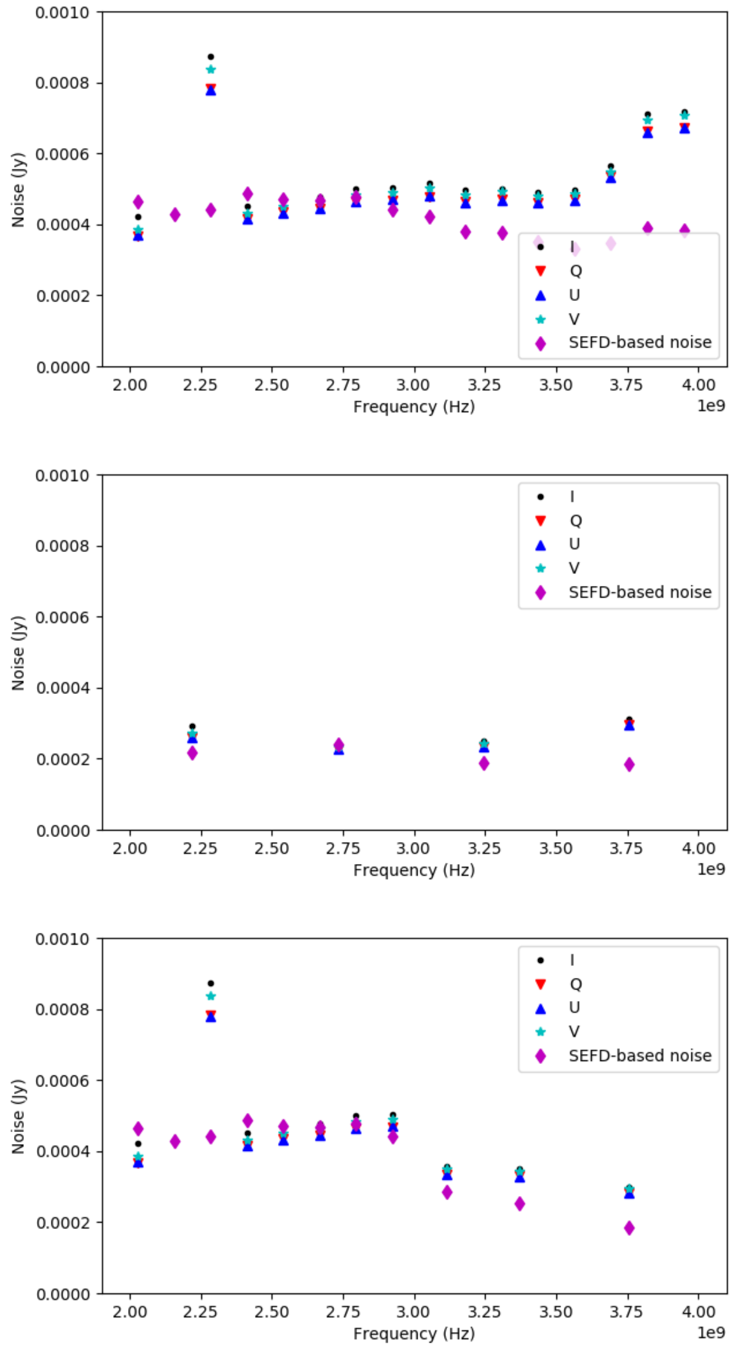

Figure 2: Noise versus frequency for each channel combination. Top, 16 planes, middle, 4 planes, bottom, 11 variable-width planes. In all cases, the magenta diamonds indicate the expected noise baed on the SEFD values in EVLA Memo 204.

3 Polarization

3.1 On-axis calibration accuracy

The on-axis polarization accuracy is determined by a number of factors. For Df calibrations, the accuracy of the leakage terms is dependent on the assumption of near-zero polarization of the leakage calibrator. Hales (2017) suggests leakage terms for an "unpolarized" calibrator with an actual 1% polarization can be obtained to 0.2% accuracy. Calibrators used were: J0713+4349, OQ208 (J1407+2827) and J2355+4950. VLASS Memo 9 (Schinzel) shows that these calibrators are variable, but typical polarizations are $< 1\%$. We thus expect any uncorrected on-axis leakage to be well within the survey requirement

The position angle is determined by the correcting the phase offset between RL and LR via reference to a standard calibrator (3C286, 3C138 or J1800+7828) of known position angle (3C286 or 3C138; J1800+7828 was used as a backup in 1.1,1.2 and 2.1, but it is variable so it is no longer observed). The position angle calibration should be accurate to $<< 1$ deg, but for reasons possibly related to uncorrected antenna tilts (Perley, personal communication) can change through transit, and is thus uncertain at the level of 2–4 deg for the VLA (Schinzel, EVLA Memo 205). Until this can be corrected, this uncertainty needs to be taken into account in the position angle error budget.

Electrons and magnetic fields in the ionosphere induce Faraday Rotation in electromagnetic waves. Although any constant offset is mostly calibrated out by the position angle calibration, the ionosphere can vary with time, particularly around dawn, and introduce a position angle uncertainty during the observation. There may be position angle errors of up to $\approx \pm 3^\circ$ from this effect (e.g. Schinzel, EVLA Memo 205).

3.2 Off-axis leakage

Spurious polarization signals can be seen off-axis in VLA observations as the primary beam responses in Stokes I, Q, U and V differ. As the polarized signal is typically small, the dominant term for this arises as leakage from Stokes I into images made from the other Stokes parameters. The VLA primary beam has been measured using holography in all four Stokes parameters, and it is thus possible to simulate the impact of off-axis leakage on VLASS data. J. Marvil took the holographically-determined polarized primary beam measurements in Q and U and produced images of the expected leakage errors in VLASS images (Figure 4). These simulations suggest that over most of the survey, leakage into Q and U is $\lesssim 0.3\%$, though at the edges of observing tiles where there is less overlap of pointings within a scheduling block the leakage may increase to $\lesssim 0.5\%$.

4 Tests on individual objects and fields

Validation of VLASS polarization in the general case is difficult, given that many polarized sources have variable polarization, and averaging over large numbers of sources is needed to ensure a robust characterization of off-axis leakage, for example. To validate the small number of images produced by the polarization scripts prior to the deployment of the pipeline, we therefore focussed on individual sources, or fields with well-characterized polarization measurements from other telescopes.

4.1 Mars

An independent measure of any systematic offset in the polarization position angle can be provided via images of resolved planetary disks. Theory and observations show that the electric vector is polarized in the radial direction around the limb of the planet due to propagation effects when the emission is transmitted and partly reflected at the planetary surface (e.g. Perley & Butler, 2013). This, then, provides a robust way to test for a systematic offset between the polarization position angle and truth.

VLASS2.1 observed Mars near opposition on 2020-08-17 (VLASS2.1.sb38530355.eb38576088.59078.34299474537). The data were processed through the VLASS calibration pipeline and then imaged in I, Q and U by S. Myers. The resulting image clearly shows the expected radial polarization pattern, and peak polarization values of about 10% (Figure 3). Although the SNR in any individual beam is not very high, by averaging the difference

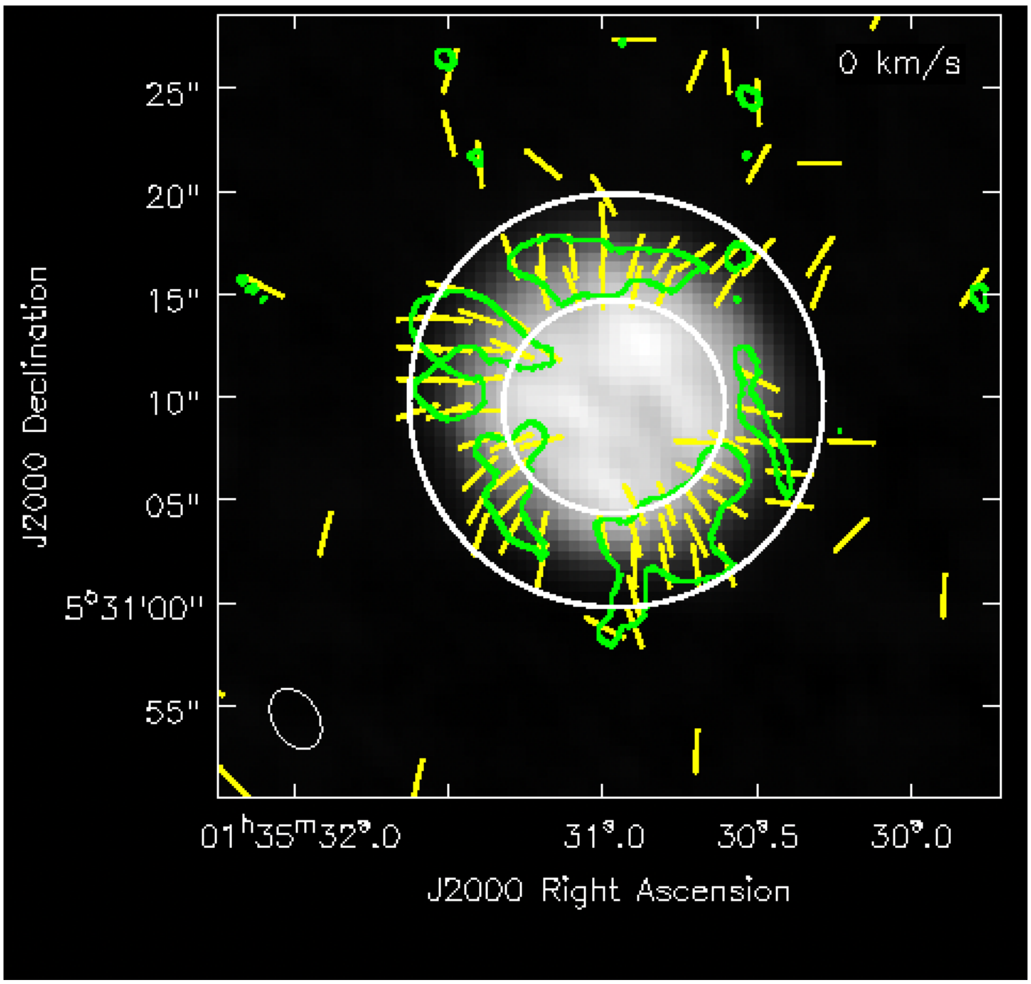

Figure 3: The polarization of Mars in VLASS. Yellow lines represent the orientation of the electric vectors, green contours are the polarized intensity at 0.0005 and 0.001 mJy/beam.

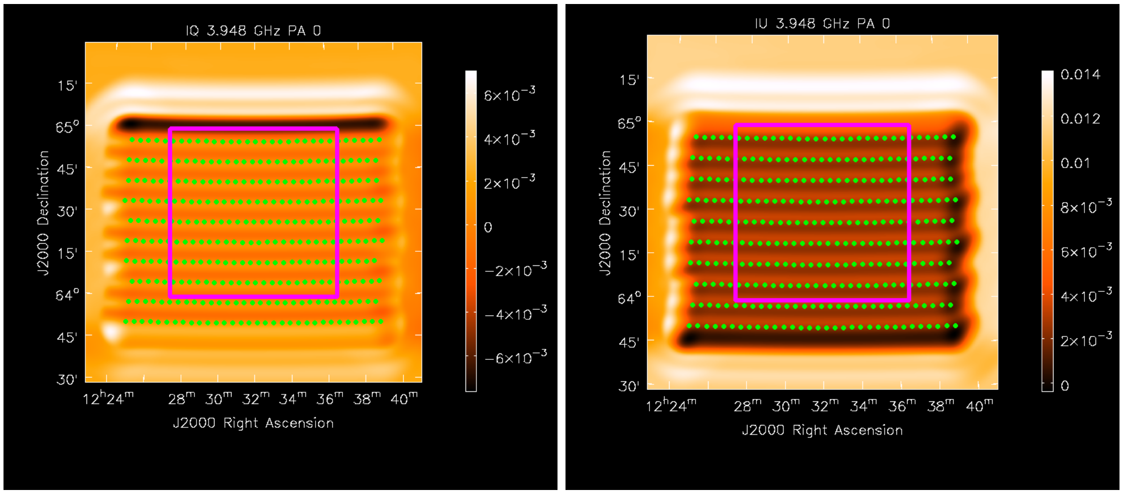

Figure 4: Predicted leakage of *left* Stokes I into Stokes Q, and *right* Stokes I into Stokes U in a VLASS mosaic image, based on holographic primary beams (J. Marvil, personal communication). The simulation covers the $2 \times 2\,\mathrm{deg}^2$ area of the images as made by the pipeline, the magenta square indicates the central $1 \times 1\,\mathrm{deg}^2$ area that is cut out to form the final VLASS image product (as the simulation is for the top of a tile the top row that is included within the square has a higher leakage magnitude in both Q and U). The green dots indicate the phase centers that were combined to make the simulation. Apart from the top of the image, which corresponds to the top of the observing tile for this image, the leakage is only $\approx \pm 0.2\%$. Note that the zero offset in the IU leakage image is thought to be an artifact of the way the leakage is calculated.

between the polar angle and the polarization PA in an annulus of radius 5–10 arcsec we can obtain a mean difference between the polar angle and the polarization vector of 0.7 ± 2 deg. There are some systematics visible, however, particularly in the Stokes Q image, where the Q polarization pattern is slightly offset from that expected from purely radial polarization due to what looks like a clean artifact, probably because the cleaning was no carried down to low enough SNR. This results in an oscillation in the difference angle with a peak-to-peak amplitude ≈ 20 degrees.

4.2 Bright source: PKS 0326-288 (J032836-284152)

The bright (1.5 Jy), extended (15-arcsec) FRII radio source PKS 0326-288 ($z = 0.109$) is imaged in J032647-283000 (tile T03t06). This source was chosen to examine residual systematic effects in the spectral index and polarization rotation measure (as it is also detected in the RM catalog of Taylor et al. (2009)). First, we calculated the spectral index map in each of the cube variants, using the position-corrected cube planes. Each plane was convolved to a common 3.5-arcsec resolution before each pixel was fit using Equation 6:

$$\log_{10} S_\nu = \log_{10} S_0 + \alpha \log_{10}(\nu/\nu_0) \tag{6}$$

The results are shown in Figure 5. This object is bright enough that any differences from the expected spectral index distribution arise from systematic effects rather than noise.

As expected, the uncorrected image (upper left) shows artifacts, including a northern lobe that steepens towards the core, and an unphysically flat spectral index at the tip of the southern lobe. When the positions are corrected (upper right) the artifacts are reduced, though the tip of the northern lobe is still unusually steep, and there is an area of unusually flag spectrum emission on the west side of the northern lobe. These issues are probably due to beam variation between the planes - although all planes are convolved to a common Gaussian, there are enough small variations in beamshape that this likely accounts for the issues. The 4-band spectral index images is clearly not as good as the 16-band, probably due to issues of varying position offset through the broader bands. Similarly, the variable width plane image, though comparable to the 16-band image has a small region of unphysically flat spectral index on the west side of the southern lobe.

The flux-weighted mean spectral indices of the source can be compared to a second-order fit in log(frequency) vs log(flux) to the literature flux values from NED at 365, 408, 1400, 2700, 5000 and 8400 GHz and the TGSS ADR (150 MHz; Intema et al., 2017) (Figure 6). This fit gives the spectral index at 3.0 GHz of -0.7673 ± 0.0005, which is reproduced well by the 16-plane cube (-0.78), but the 4-plane and variable plane cubes recover slightly flatter values of -0.70 and -0.69, respectively. Although this is not an ideal test as the steeper parts of the emission may have been masked in the image, it does suggest that the 16-plane images are significantly more accurate. All cubes are nevertheless much more accurate than the corresponding value for the AW32 SE continuum image (-0.99) and better than the Mosaic gridder (-0.85).

We next examined the polarization properties of this source. For the purposes of validation we needed to show that the polarization properties were consistent with expectations of the properties of FRII sources in the literature, and that the overall RM was consistent with the measurement of Taylor et al. (2009) at 1.4 GHz (34.3 ± 1.8 rad m^2).

In Figure 7 we plot the polarization properties at the peak position of the brightest image component (such a plot may be useful for QA purposes). For this source, there is no evidence for depolarization across the band, and a simple foreground screen model works well. Fitting this model to the entire source (Figure 8) we find a median RM of 30.2±2 in the 16-plane, 32.8±2 in the 4-plane and 27.1±2 for the variable width cube. So in this analysis, the 4-plane cube behaves best, the 16-plane is next best, and the variable plane is slightly worse. Examination of the fit for the variable-plane cube (Figure 7) suggests this is due to the noisier low frequency planes getting more weight (the fit is not weighted by he RMS).

4.3 Intermediate source: J032541-285548

Also in image J032647-283000 is the source J032541-285548. With a total flux density $\approx$ 41 mJy, it is more representative than PKS 0328-288. It is extended by 10-arcsec, with two steep spectrum lobes. We performed the same analysis as above for this source. The conclusions are similar to those for PKS 0328-288, namely that the 4-plane cube still shows some systematics, but that the 16-plane and variable-width plane cubes give comparable results that look physically reasonable. Although the RM estimate is noisy, both the variable and 16-plane cubes obtain estimates of $\approx 15 \pm 30$radm^{-2} for the RM to the source, consistent with the Milky Way screen in front of PKS 0326-288, whereas the 4-plane version gives 8 ± 1radm^{-2}, with the unreasonably small error bars probably reflecting the low number of degrees of freedom in the fit. All cubes indicate a significant degree of depolarisation in the Southern lobe (by about a factor of 3 across the band).

4.4 Faint source: J032648-284736

We also examined a example of a faint object, J032648-284736, with a total flux density $\approx$ 9 mJy and also a size of 10-arcsec. At this level, the SNR of individual beams in the 16-plane cube is low ($\approx 1-3$ mJy/beam compared to an RMS $\approx$ 0.5 mJy. The SNR is particularly low in the high frequency channels, this seems to lead to an underestimate of the flux-weighted spectral index (-0.55) compared to the other two plane choices, which agree well (-0.94 for the variable-width cube and -0.98 for the 4-plane cube). Figure 9 shows the spectral index images for the three different cubes.

Polarimetry on such a faint source is difficult, the only one of the three cubes to show detectable polarization in the source was the variable plane cube, where the center of the source is detected in polarization at $\approx 2\sigma$.

4.5 Tests by CIRADA

The J032647-283000 test cube was also run through CIRADA's polarization software and analysed by C. van Eck and J. West (personal communication). By using RM synthesis, they were able to obtain polarization estimates for fainter sources. To produce better statistics on the polarization properties, three additional fields were selected on the basis of having the most previously published RMs while covering both northerly and southerly declinations. These three fields (J032647-283000, J032647-283000 and J232146+503000) have a combined 40 RMs previously published between 1980 and 2021. One small difference between the J032647-283000 test cube and the three additional cubes was that the J032647-283000 test cube had all planes (frequency and Stokes) made as 48 individual images, whereas the additional cubes were made the way the

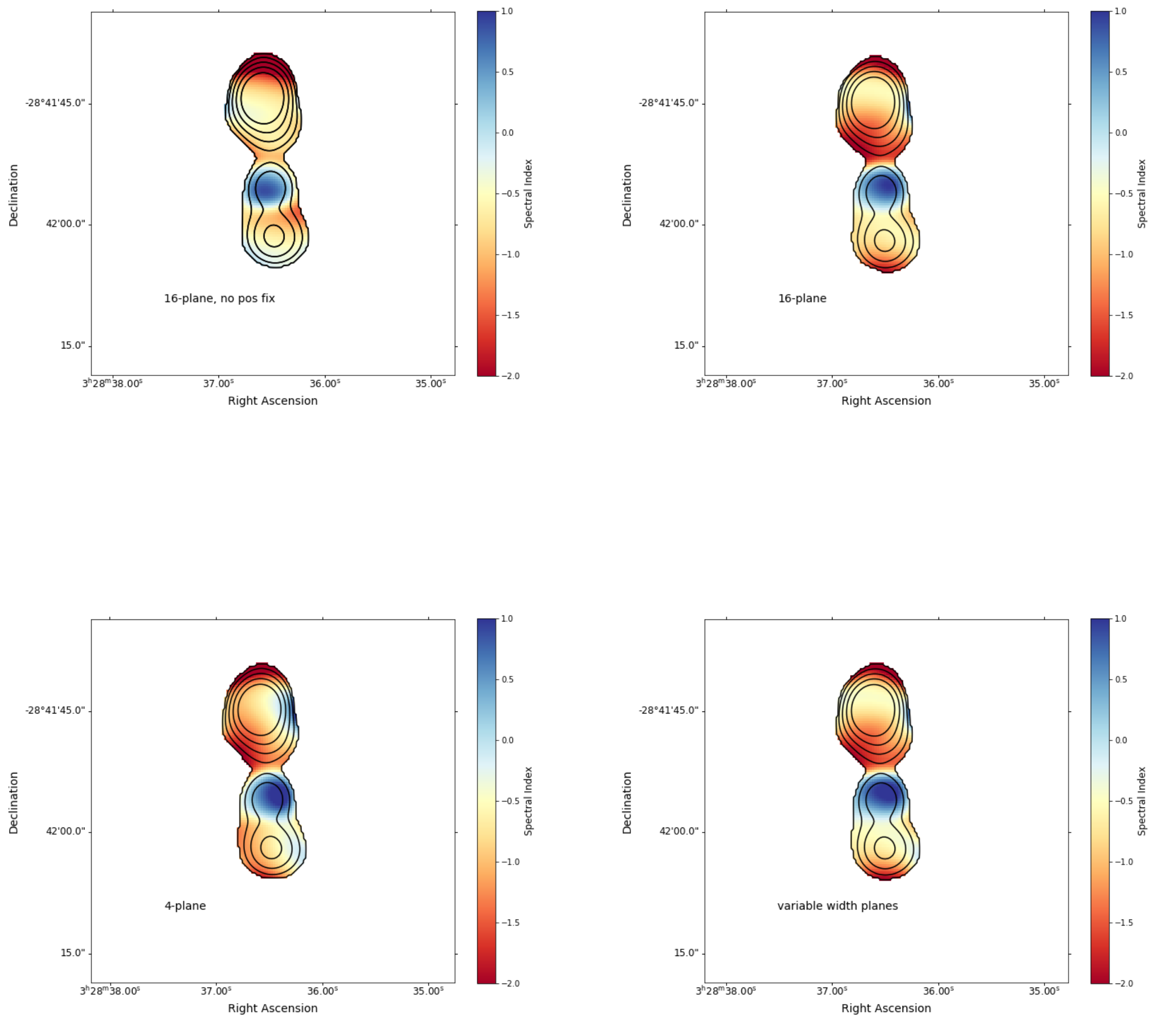

Figure 5: Spectral index images from cubes for the bright source PKS 0326-288. Upper left, 16-plane with no position correction, upper right, 16 plane with position correction, lower left, 4-plane with position correction and lower right, variable width planes.

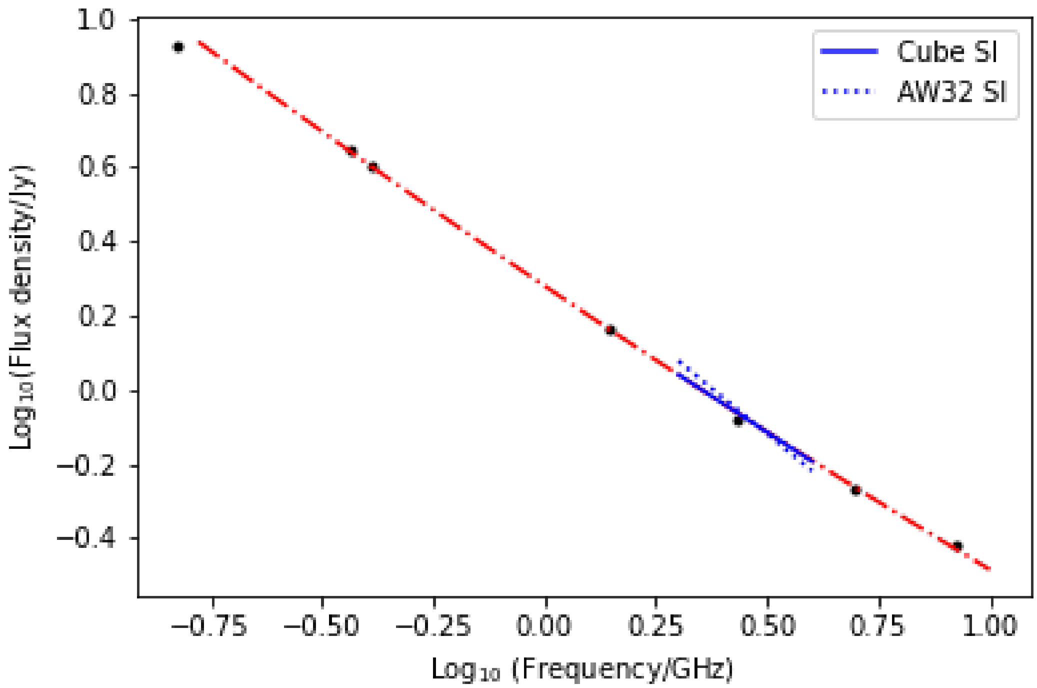

Figure 6: Spectrum of the bright FRII source PKS 0326-288 from NED. The red dot-dashed line is a 2nd-order fit in $\log(\nu)$. The blue solid line is the flux density weighted spectral index from the 16 plane cube, the blue dotted line is the same from the AW32 SE continuum image.

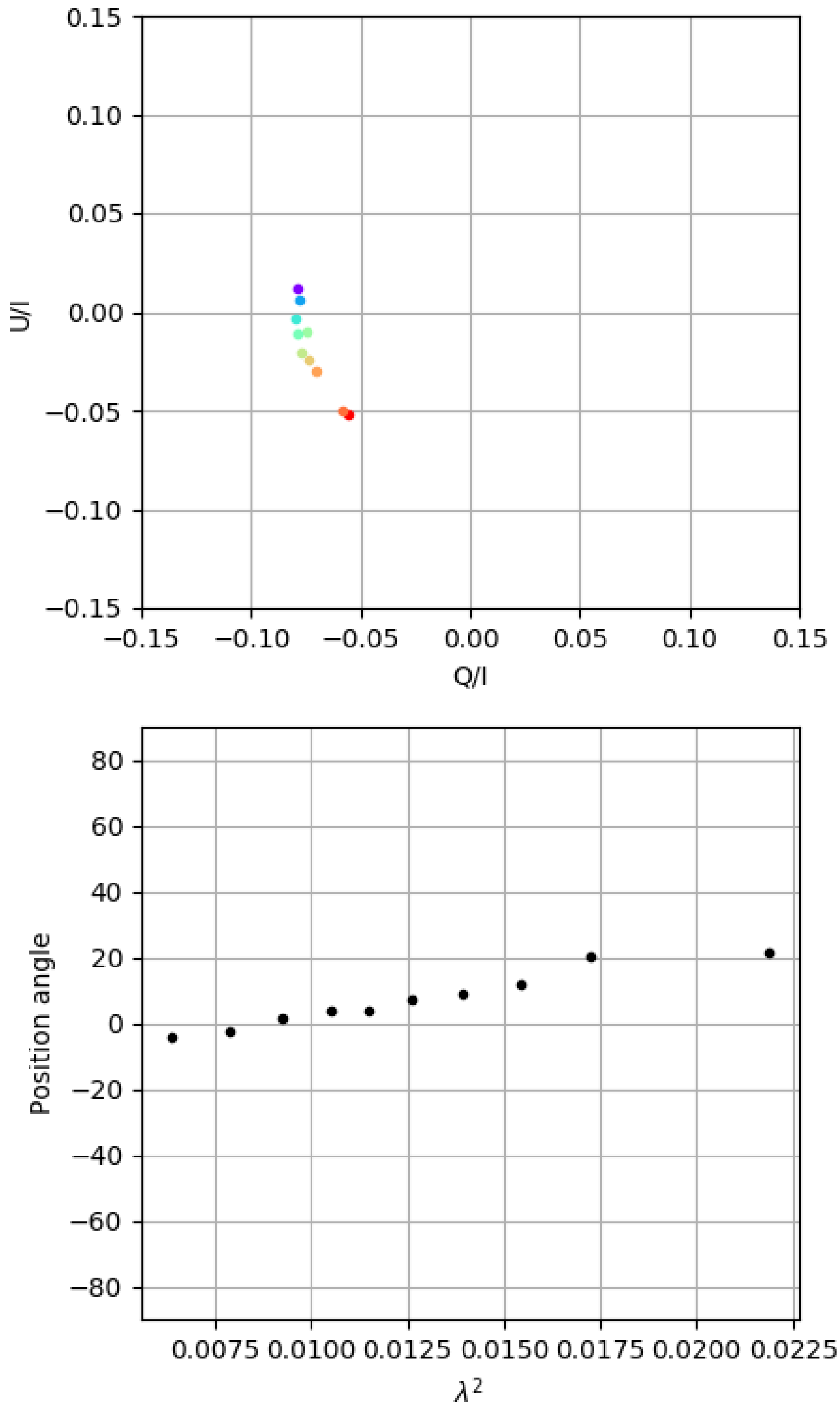

Figure 7: Q versus U and polarization angle versus λ^2 plots for the brightest component peak in the variable cube of PKS 0326-288. The points in the QU plot are colored red to violet depending on frequency.

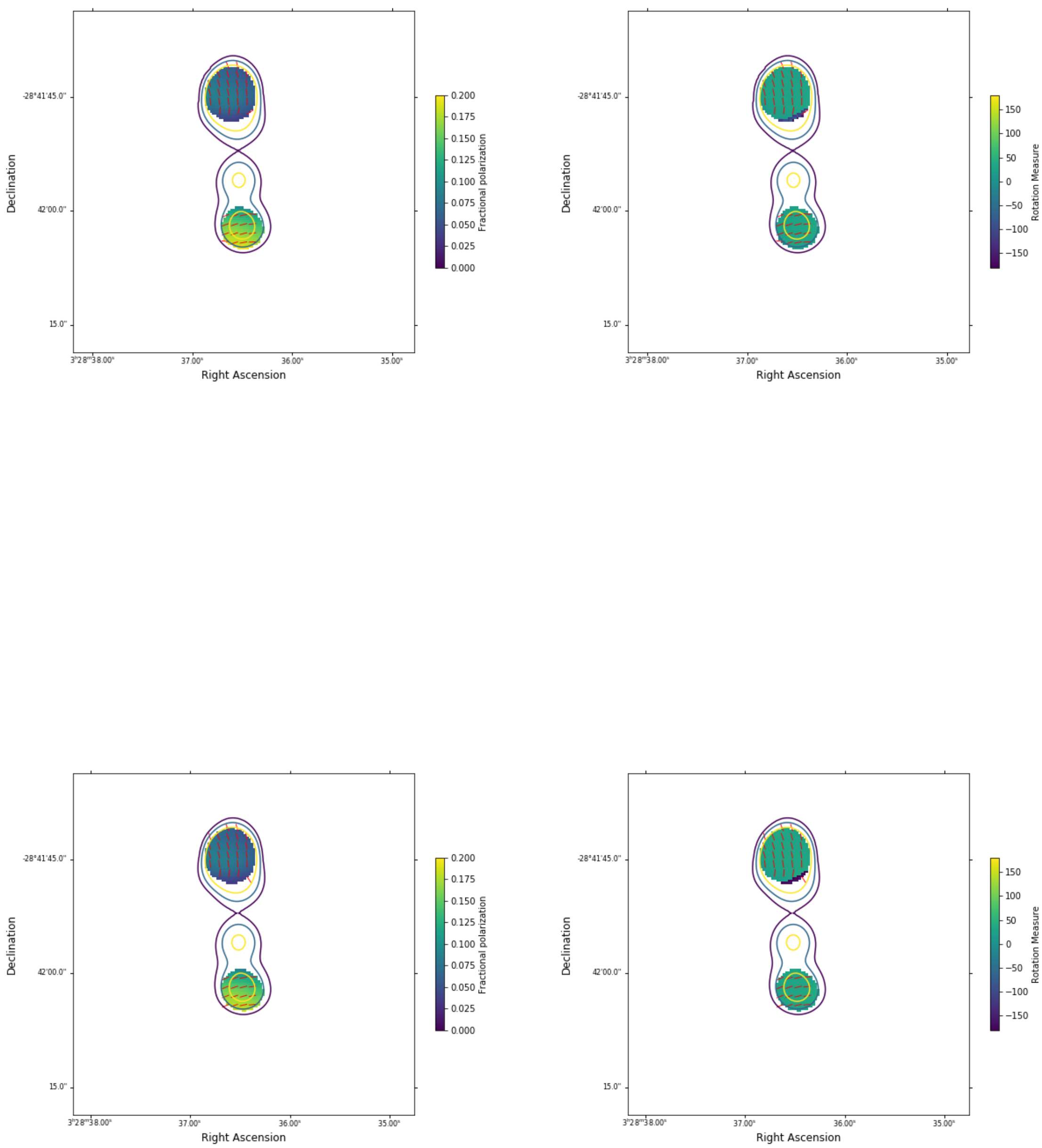

Figure 8: Polarization fraction and rotation measure for the 16-plane image (top) and 4-plane image (bottom) of PKS 0326-288.

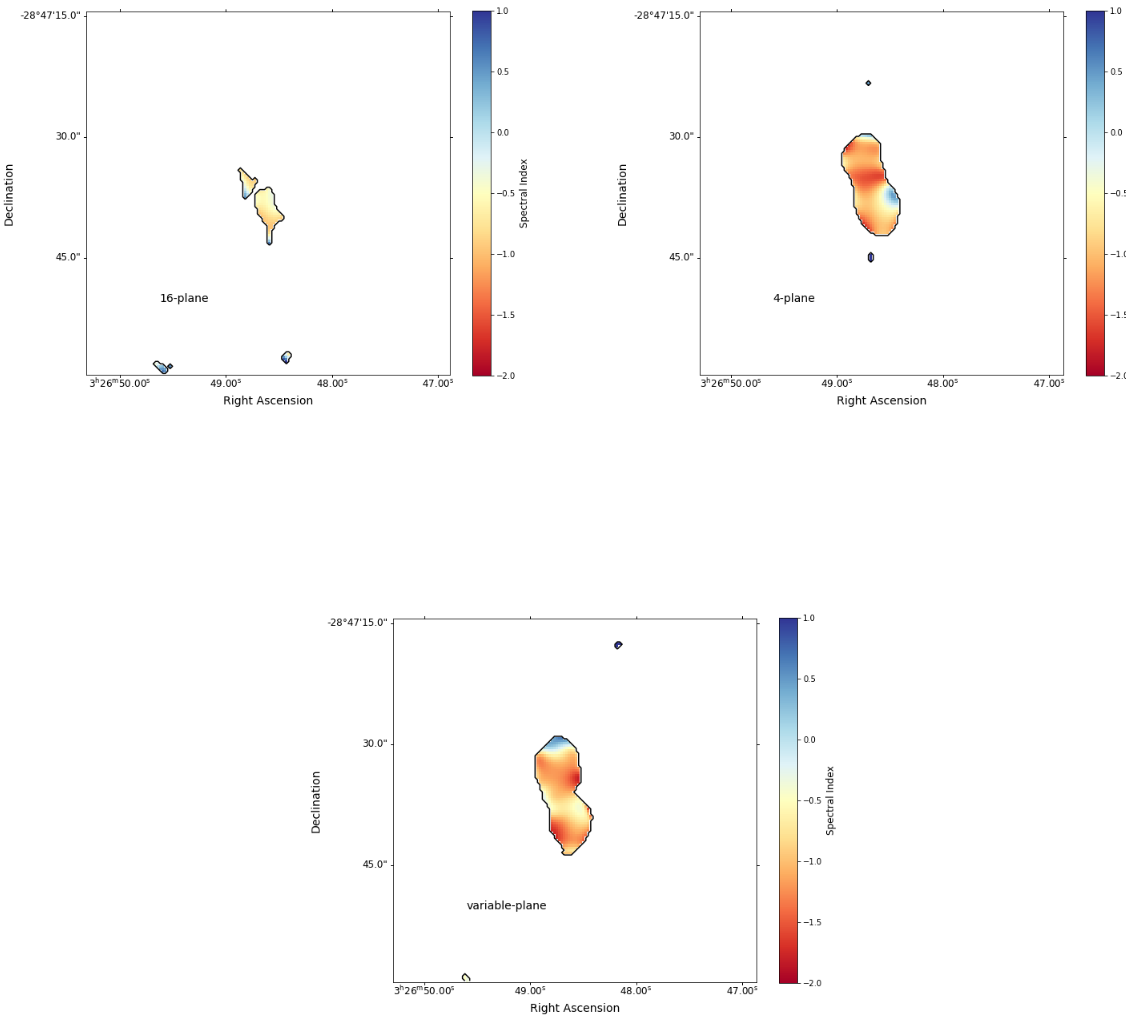

Figure 9: The faint (9 mJy) source in spectral index. Top left, 16-plane cube, top-right 4-plane cube, bottom variable width cube (note that all cubes are masked at 1 mJy/beam in each plane, hence the irregular shape of the 16-plane image where the noisier individual channels sometimes dip below 1 mJy in the lower brightness regions of the source).

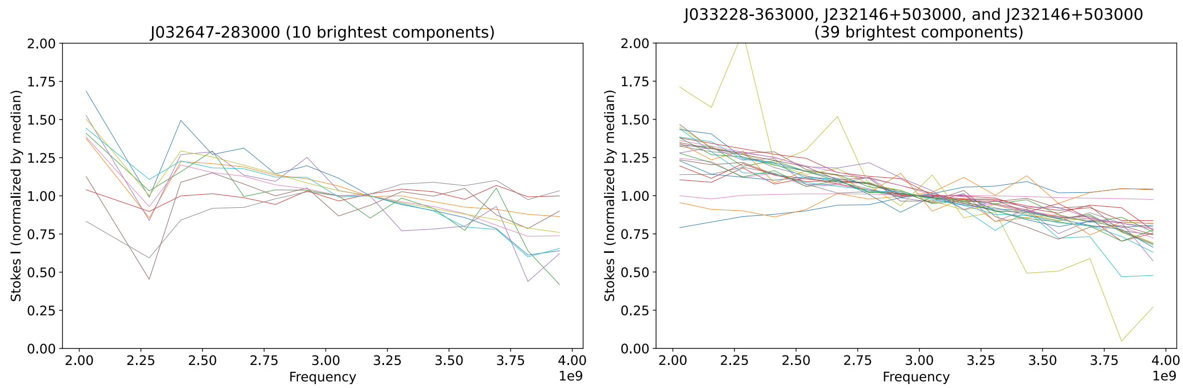

Figure 10: Output from the CIRADA analysis of the test cubes, showing Stokes I spectra of the ten brightest source components in the J032647-283000 field on the left, and of the 39 brightest components in the additional three test fields on the right.

pipeline will make them, namely as 16 Stokes I, Q, U, V cubes. This should make no difference to the image quality.

The new cubes were also processed through the CIRADA polarization pipelines. Figure 10 shows the spectra of the brightest source components for both the initial (J032647-283000) cube and the three follow-up cubes. The J032647-283000 cube spectra show discontinuities due to severe RFI in some spectral windows (2.28 and 3.78 GHz); this is not present in the follow-up cubes. As discussed in 5.2 we will need to be able to flag such channels as bad (or reject them altogether) for any data release. The CIRADA pipeline identified 39 source components with polarized intensity greater than 5σ in the four cubes (out of 187 components present in the VLASS QL catalog). The positions of these components, in comparison with the positions of the previously published RMs, is shown in Figure 11. Note: (1) in the J033228-363000 field (left panel), the three previously published RMs without VLASS counterparts were from Anderson et al. (2015) which was more sensitive in polarization than VLASS; (2) the cluster of measurements in the lower right of the J141718-363000 field (centre panel) come from a very large double-lobed radio galaxy where different observations have reported RMs at different positions (and at different resolutions), and (3) the position offsets between VLASS and published RM are generally not significant as some of the older RMs have very limited coordinate precision.

A comparison of the VLASS and published RM values is shown in Figure 12. The agreement is very good by the standards of such comparisons – some additional scatter beyond the reported uncertainties is expected due to effects like ionospheric Faraday rotation, Faraday complexity, observation resolution, etc. Three components show strong discrepancies in RM (much larger published RMs compared to VLASS); these were investigated and found to be cases where the published catalogs were likely to have problems (sources resolved in VLASS but blended/unresolved in the published measurements, complicated source morphology, etc), so these are not considered evidence of any problems with the VLASS polarization data.

4.6 HII region: IRAS Z20376+4109

This source on image J203945+413000 (tile T21t21) is identified with a bright HII region/protostar in SIMBAD. We therefore expect it to be dominated by thermal emission and to have zero polarized flux, so we use this source to check for leakage, both on- and off-axis. It has a typical brightness in VLASS of ≈ 20 mJy/beam, and the 46-arcsec diameter source has a measured flux total density ≈ 800 mJy.

A limit on the on-axis leakage (requirement SCI_BDP-21) was estimated by measuring the flux density within a 46-arcsec diameter aperture in Stokes I, Q and U in the 4-plane cubes (as they have the lowest thermal noise). The limits obtained on the on-axis leakage are < 0.06, < 0.10, < 0.22 and $< 0.29\%$ in spectral windows 2-5, 6-9, 10-13 and 14-17, respectively, compared to a requirement of 0.75% and a goal of 0.25%. The quality of the polarization calibration will vary between scheduling blocks, but assuming this observation was typical the on-axis leakages are well within requirements and probably meet the survey goal.

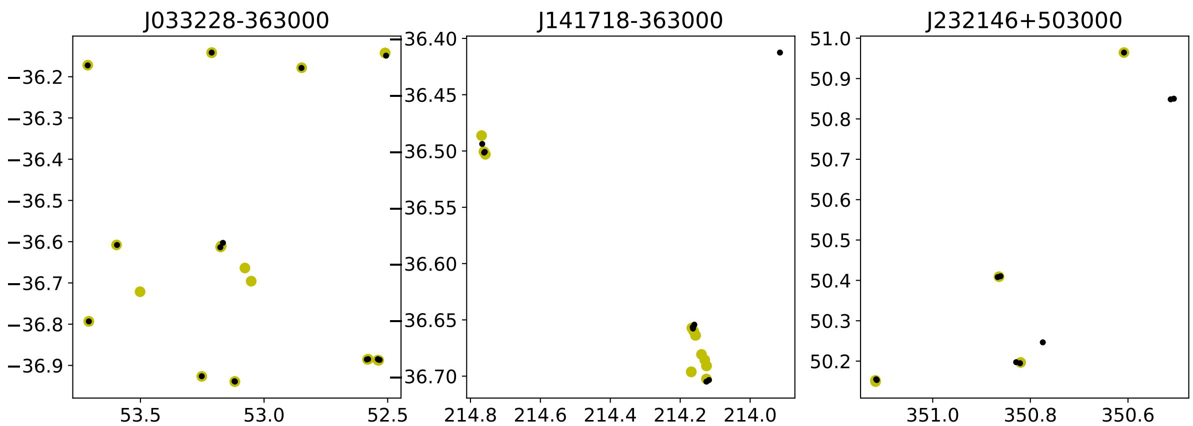

Figure 11: Positions of the 39 polarized components found in the follow up cubes (black points). Previously published RMs are marked as yellow dots.

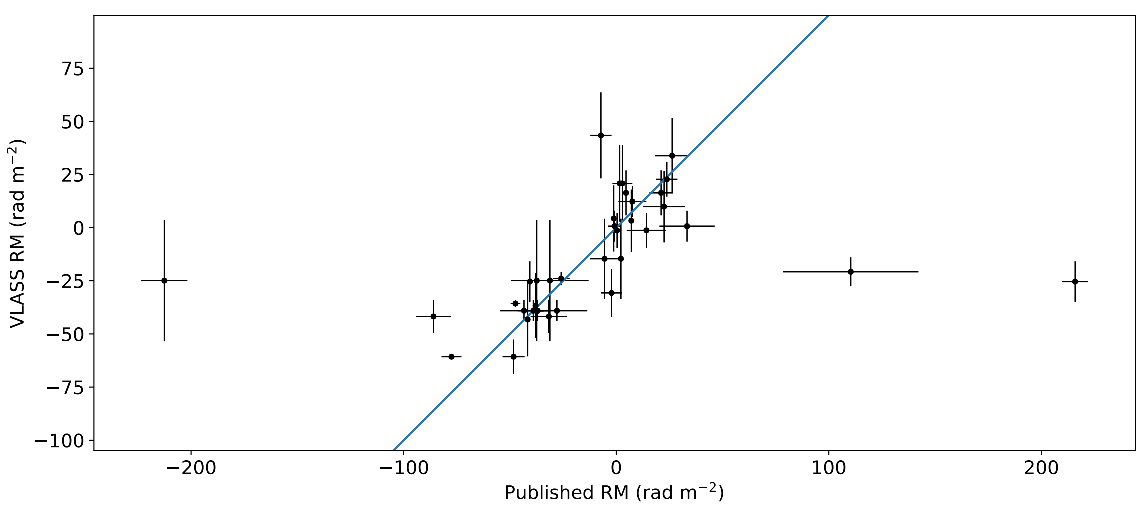

Figure 12: Comparison of VLASS and published RMs for the three follow-up cubes, with the 1:1 agreement line marked.

Placing a meaningful limit on the off-axis leakage (requirement S4) is more difficult, as the scale on which such a leak would occur is unclear. The source spans from 41:19:40 to 41:20:20 in declination, for comparison, the nearest scan rows are at 41:16:48 and 41:24:00, placing this object between scan rows, where we might expect the off-axis effects to be largest. We do see evidence of an off-axis leakage in Stokes V (note that V images are not an official VLASS product and the off-axis leakage observed is thus not to be compared to the survey requirements, which apply only to linear polarization). The V-leakage manifests as spikes aligned with the PSF starting at about 2.3 arcmin from the source.

In order to place a limit on the off-axis leakage in Stokes Q and U, where no leakage was visible in the images, we placed our apertures at the positions in each of the 4-plane channels where the V leak was a maximum (Figure 13), measured the total fluxes in those apertures and divided by the Stokes I flux. This leads to limits on the off-axis leakage of $< 0.07\%$, $< 0.12\%$, $< 0.03\%$ and $< 0.33\%$ in spectral windows 2-5, 6-9, 10-13 and 14-17, respectively, compared to a requirement of 0.75% and a goal of 0.25%. In V, the off axis leakage is only 0.6% in the worst affected data (spectral windows 14-17) and thus V could be released and satisfy the survey requirements. One caveat to this approach is that although the HII region has a high total flux, it is extended, which might lead to a small-scale leakage pattern averaging out. However, as we expect the characteristic scale of the leakage pattern to be of order primary beam, not synthesized beam variations, this approach is probably valid.

5 QA procedures

5.1 Calibration

Diagnostic plots in the weblog can be used to assess the quality of the on-axis polarization calibration. Calibration for VLASS 2.1 onwards used the Df calibration scheme, where the polarization leakage terms were determined through the observation of an unpolarized calibrator. Plots of amplitude versus frequency for the leakage calibrator can then be checked that the values in the cross polarization (RL,LR) are close to zero.

5.2 Imaging

The effect of RFI can be much more pronounced in the narrow cube channels than in the wideband continuum, as RFI tends to be concentrated in specific frequency bands. This can lead to some individual channels having a large fraction of flagged data and/or residual unflagged RFI. We will therefore need a way to identify such channels (typically through RMS and/or an unusual beamsize) and either flag them, or, in the worst cases, QA reject them.

6 Summary

The analysis in this Memo suggests that spectral indices and polarization properties can be recovered within the survey requirements in all three cube options for sources above 10 mJy/beam in Stokes I. Below these levels, the 4-plane and variable cubes seem to work for spectral index to ≈ 3 mJy/beam in Stokes I, but the 16-plane cubes lack SNR at the higher frequencies at these brightness levels. For high precision work at high SNR, the 16-plane cubes are the most accurate, limited only by small variations in the beams as a function of frequency that remain after smoothing to a common resolution.

Away from the tile edges, we find no measurable leakage from Stokes I into Stokes Q and U, to a limit of $< 0.3\%$ both on- and off-axis. Although more work is needed to characterize the performance over a larger area of the survey (particularly near the tile edges), the polarization products are very likely to satisfy the survey requirements (Table 2). Off-axis leakage in Stokes V is visible, but only at $\approx 0.6\%$, thus Stokes V is likely to be scientifically useful.

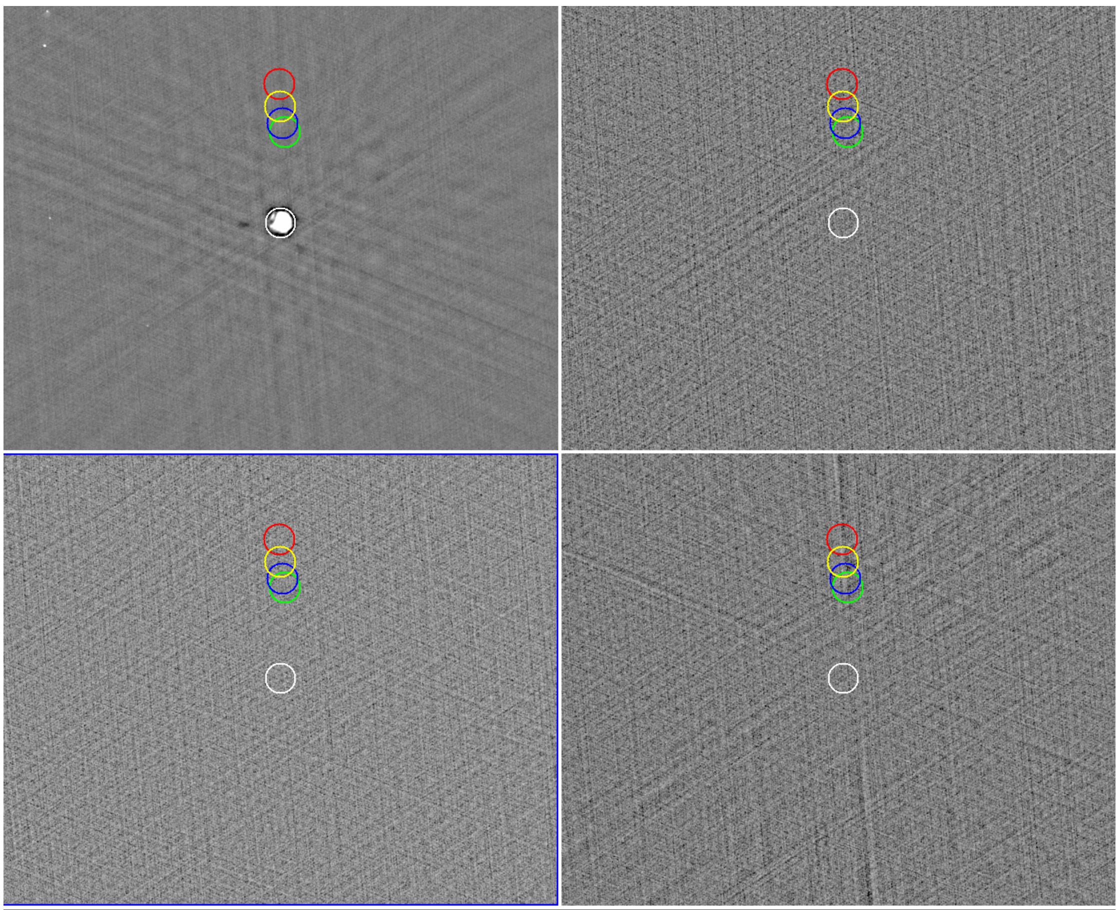

Figure 13: Polarization leakage evaluation around the HII region IRAS Z20376+4109. On the upper left is the Stokes I image, upper right Stokes Q, lower left, Stokes U and on the lower right the Stokes V images (spectral windows 10-13). The white circle shows the 46-arcsec region around the source, used to constrain the on-axis leakages.The four colored circles show the 46-arcsec diameter apertures where the Stokes V off-axis leakage is maximized in spectral windows 2-5 (red), 6-9 (yellow), 10-13 (green) and 14-17 (blue). The total flux densities in these apertures were used to measure the Stokes V leakage and constrain the leakages in Q snd U.

Table 2: Tablulation of validation results versus requirements for cube images (including in-band spectral indices and polarization properties

Requirement	Goal/Required value	Achieved value	How tested
Polarimetry: on-axis QU leakage (SCI-BDP-021)	0.25%/0.75% over 90% area	$< 0.3\%$	HII region
Polarimetry: angle (SCI-BPD-022)	2 deg/5 deg† over 90% area	± 2deg.	Mars observation
Polarimetry: off-axis QU leakage (S4)	0.25%/0.75% over 90% area	$< 0.3\%^{*}$	HII region
Polarimetry: mosaic accuracy (S5)	5%/10% in Q, U		Comparison to calibrators/ptd
Common beamsize (S6)	4.5/5 arcsec	4.5 arcsec	inspection
Minimum # cube planes (S7)	> 12	> 12	inspection
In-band polarization accuracy (S8)	RMS of fit <5%/10%	5%	Fit to J0328 16-plane peak
Spectral index: extended src. (S10)	within thermal noise	$\pm 0.1 - 0.5^{\ddagger}$	Compared to expected source properties

* may be higher near edge of tiles.

† original requirement of 2 deg. probably cannot be achieved in practice due to change in polarization PA during transit (EVLA Memo 205).

‡ limiting factor appears to be the variation in beamshape with frequency. Cube spectra nevertheless seem to be more reliable that those from continuum imaging, and should be used if feasible.

7 Recommendations

- The 16-plane cube option gives the most accurate results and is sensitive to the highest RM, and thus is recommended for production.
- Quality assessment (QA) needs to be performed on a per-plane basis, with planes heavily affected by RFI being flagged and/or QA-rejected.
- Stokes V products appear good enough to be scientifically useful. Archival storage of Stokes V is suggested if the budget can be found.

References

Anderson, C. S., Gaensler, B. M., Feain, I. J., & Franzen, T. M. O. 2015, ApJ, 815, 49

Hales, C. A. 2017, AJ, 154, 54

Intema, H. T., Jagannathan, P., Mooley, K. P., & Frail, D. A. 2017, A&A, 598, A78

Perley, R. A., & Butler, B. J. 2013, ApJS, 206, 16

Taylor, A. R., Stil, J. M., & Sunstrum, C. 2009, ApJ, 702, 1230

A Effects of leakage in the circular basis

The effect of uncorrected leakages is assessed as follows: assume a leak of $\delta_L L$ leaks into R, and a leak of $\delta_R R$ leaks into L (where δ_L, δ_R are complex numbers). Then:

$$< RR >=< RR > +\delta_L < LR > +\delta_L < RL > +O(\delta^2) \tag{7}$$

$$< LL >=< LL > +\delta_R < RL > +\delta_R < LR > +O(\delta^2) \tag{8}$$

$$< RL >=< RL > +\delta_L < LL > +\delta_R < RR > +O(\delta^2) \tag{9}$$

$$< LR >=< LR > +\delta_L < LL > +\delta_R < RR > +O(\delta^2). \tag{10}$$

Forming Q, U and V according to Equations 1-4, treating δ_L, δ_R as error terms, and assuming $< RR >\sim< LL >$ and $< RL >\sim< LR >$ we have:

$$\Delta(Q) \sim \Delta(U) \sim< RR > \sqrt{\delta_L^2 + \delta_R^2} \tag{11}$$

$$\Delta(V) \sim < RL > \sqrt{\delta_L^2 + \delta_R^2}. \tag{12}$$

As the cross-hand correlations are much smaller than the parallel-hand correlations, this suggests that the effect of leakages in V is much smaller than that in Q and U (at least in the on-axis case, off-axis the beam squint can lead to high values of V leakage). Thus, any V leakage seen in the images that is on axis is likely due to issues with the Stokes I calibration, i.e. an offset of the $< RR >$ and $< LL >$ solutions, rather than a problem with the leakage (D-term) calibration.

B Optimized channels for Faraday rotation

An interesting question is what the optimal channel spacings are if we are interested in having channels with a uniform RM_π across the band, regardless of spectral window boundaries. We can calculate these approximately as follows. First, for a desired number of channels $n_{\rm ch}$ the spacing in wavelength squared, $\Delta(\lambda)^2$ for these is:

$$\Delta(\lambda)^2 = \frac{\lambda_1^2 - \lambda_2^2}{n_{\rm ch}} \tag{13}$$

then their spacing in wavelength, $\Delta\lambda$ is:

$$\Delta\lambda \approx \frac{\Delta(\lambda^2)}{2\lambda}. \tag{14}$$

Discretizing this, we obtain $(n_{\rm ch} + 1)$ channel boundaries λ_i^b:

$$\lambda_{(i+1)}^b \approx \lambda_i^b - \frac{\Delta(\lambda^2)}{2\lambda_i}. \tag{15}$$

We fix $\lambda_1^b = 1.964\,\mathrm{GHz}$ at the lower end of the VLASS bandwidth and $\lambda_{n_{\rm ch}+1}^b = 4.012\,\mathrm{GHz}$ at the upper end. λ_i is defined by:

$$\lambda_{(i+1)} = \lambda_i^b - \frac{\Delta(\lambda^2)}{2\lambda_i} \tag{16}$$

with $\lambda_1 \approx \lambda_1^b - \frac{\Delta(\lambda^2)}{4\lambda_1^b}$. This discrete approximation improves as $n_{\rm ch} \to \infty$. In Table 3 we list an example for 16 channels for which $\Delta(\lambda^2) \approx 0.011\,\mathrm{m}^2$, corresponding to $RM_\pi \approx 2900$ in each channel.

Channel	Start frequency (GHz)	End frequency (GHz)
1	1.964	2.012
2	2.012	2.065
3	2.065	2.121
4	2.121	2.182
5	2.182	2.249
6	2.249	2.322
7	2.322	2.403
8	2.403	2.493
9	2.493	2.594
10	2.594	2.708
11	2.708	2.839
12	2.839	2.900
13	2.900	3.167
14	3.167	3.380
15	3.380	3.642
16	3.642	4.012

Table 3: Near-optimal channelization for a 16-channel sampling of the VLASS 1.964–4.012 GHz bandwidth in which each channel corresponds to the same $\Delta(\lambda^2) \approx 0.011\,\mathrm{m}^2$.